Available online at www.sciencedirect.com
ScienceDirect
Acta Materialia 57 (2009) 2583–2591
Acta MATERIALIA
www.elsevier.com/locate/actamat

Evolution of thermal properties of EB-PVD 7YSZ thermal barrier coatings with thermal cycling

Tyler R. Kakuda [a], Andi M. Limarga [b,*], Ted D. Bennett [a], David R. Clarke [b,a]

[a] Department of Mechanical Engineering, University of California, Santa Barbara, CA 93106-5070, USA
[b] Materials Department, University of California, Santa Barbara, CA 93106-5050, USA

Received 28 August 2008; received in revised form 9 February 2009; accepted 11 February 2009
Available online 13 March 2009

Abstract

During high-temperature exposure, the microstructure of thermal barrier coatings evolves, leading to increased thermal conductivity. We describe the evolution in the thermal properties of a 7 wt.% Y_2O_3 stabilized ZrO_2 electron beam-physical vapor deposited (EB-PVD) thermal barrier coating with thermal cycling between room temperature and 1150 °C until failure. The thermal diffusivity and conductivity of the coating were evaluated non-destructively based on the analysis of its photothermal infrared emission. Although the coating density does not increase significantly with thermal cycling, the thermal diffusivity and conductivity of the coating increased substantially, particularly during the first 20 1 h cycles. The values then approach a limiting value. Complementary Raman spectroscopy suggests that the increase is accompanied by a reduction in the defect concentration in the coating and that there is also a correlation between the width of the Raman lines and the thermal conductivity.

Keywords: Thermal barrier coating; Thermal properties; Thermal cycling

1. Introduction

Thermal barrier coatings (TBCs) are increasingly being applied to metallic components in the hottest sections of turbine engines to provide a low thermal conductivity barrier to heat transfer from the hot gas to the surface of alloy components [1]. The introduction of TBCs since the early 1990s has allowed the turbine inlet temperatures to be increased dramatically, improving the efficiency of engines without increasing the surface temperature of the coated components. A lower alloy surface temperature is also beneficial in extending the creep and oxidation life of the coated metallic components [2].

The current coating material of choice, with a nominal composition of 7–8 wt.% Y_2O_3 stabilized ZrO_2, has a relatively low intrinsic thermal conductivity [3,4] and further conductivity reduction is achieved by incorporating porosity and microcracks during deposition. During high-temperature service, the microstructure of the coatings can change, and the coatings can also undergo densification. These processes have been considered to be the primary reason for the increase in thermal conductivity observed during prolonged annealing at high temperatures [5–7]. The increase in thermal conductivity during service is undesirable since it results in an increase in the alloy surface temperature and increased heat flux through the component, decreasing the turbine thermal efficiency. For this reason there is interest in understanding the mechanisms responsible for the increase in thermal conductivity .

The thermal conductivity of TBCs is typically measured by performing flash measurements on coated buttons of superalloy of known properties, on free-standing coatings, or, occasionally, on coatings deposited on inert substrates such as sapphire [6–9]. One difficulty encountered in such measurements is that the properties change over time at high temperatures and several phenomena, such as densification, are dependent on the thickness and thermophysical

* Corresponding author. Tel.: +1 805 893 5833; fax: +1 805 893 3882.
E-mail address: limarga@engineering.ucsb.edu (A.M. Limarga).

1359-6454/$36.00 © 2009 Acta Materialia Inc. Published by Elsevier Ltd. All rights reserved.
doi:10.1016/j.actamat.2009.02.019

properties of the substrate [10]. As a result, the measured thermal conductivity of a free-standing electron beam-physical vapor deposited (EB-PVD) TBC is generally not the same as when the TBC is attached to a metallic coupon [9]. Another approach for determining thermal conductivity has been utilized by the NASA group who measured the temperature across the thickness of a coating under steady-state high heat flux [5,11], i.e. the conditions produced by a CO_2 laser heating the coating surface and air cooling of the back of the substrate. Their technique requires calibration of the laser heat flux and the simultaneous measurement of the coating surface and the metal backside temperatures with infrared pyrometers. In this manner, the thermal conductivity can be directly determined from the temperature gradient across the coating without having to determine the TBC density. While very useful, particularly for measurement of the thermal conductivity at high temperature, the method is difficult to implement on components that have complex shapes and internal cooling.

In this contribution, we discuss the evolution of thermal properties of 7YSZ EB-PVD TBCs deposited on a single-crystal nickel-based superalloy subject to thermal cycling between room temperature and 1150 °C. A non-destructive front surface measurement of coating thermal properties, based on the "phase of thermal emission" technique, is utilized [12]. Complementary Raman spectroscopy measurements are also reported: Raman spectroscopy is sensitive to the presence of point defects and it has been reported that the Raman bands from 7YSZ EB-PVD coatings narrow with annealing at high temperatures [13].

2. Materials and methods

2.1. Material and thermal cycling experiment

The coatings investigated in this study were provided by Howmet Corporation in the form of standard furnace cycle test (FCT) specimens consisting of a 140 μm thick EB-PVD 7YSZ coating deposited on a platinum-modified, nickel-aluminide-coated, single-crystal superalloy (25.4 mm diameter, 3 mm thick). The TBC coupons were cycled until failure from room temperature to 1150 °C in ambient atmosphere. Each cycle consisted of 1 h exposure at 1150 °C and 10 min cooling to room temperature. The heating and cooling rates were approximately 200 °C min^{-1}. The specimen was periodically removed from the thermal cycle rig for thermal property and Raman spectroscopy measurements.

2.2. Thermal property measurements

The thermal properties of the coating were evaluated by the phase of photothermal emission analysis (PopTea) method [12], a non-destructive thermal property measurement with the potential for monitoring serviceable parts. While PopTea is, in essence, a thermal diffusivity measurement, values of the coating density and thermal conductivity can also be determined from the same analysis. Unlike other diffusivity techniques, the surface does not have to be painted with carbon or some other high-emissivity coating. The only knowledge of the TBC system required is the coating thickness and thermal properties of the alloy on which the coating is deposited.

The experimental procedure for PopTea is a derivative of a more general family of modulated photothermal measurements [14,15] in which the coating is heated with a modulated 100 W CO_2 laser and the thermal (infrared) emission from the coating measured. An advantage of this heating method is the ability to control the depth of transient heat transfer, the thermal penetration depth ($l \sim \sqrt{\alpha/f}$), with the laser modulation frequency (f). Phase of thermal emission measurements utilize the interaction of the thermal penetration depth with the known thickness of the coating to determine the coating diffusivity (α). The phase of emission is determined by comparing the reference waveform of the laser (signal 1, Fig. 1) with the waveform from the infrared detector (signal 2, Fig. 1). Infrared thermal emission from the coating is collected and focused onto the detector with an elliptical mirror. The detector operates in the mid-infrared regime (2–5 μm), well outside the range of the laser (10.6 μm). The phase of emission (the phase-lag between signals 1 and 2) is recorded using a data acquisition PCI card.

Phase of emission measurements were made at various modulation frequencies, corresponding to a range of thermal penetration depths in the coating. Post-measurement analysis consisted of fitting the data set to a combined heat transfer and radiation model reported in detail elsewhere [16]. In this model the temperature field is derived from the periodic temperature field in the coating. Three sources of thermal radiation emission are considered: the coating surface, the alloy surface underneath the coating and emis-

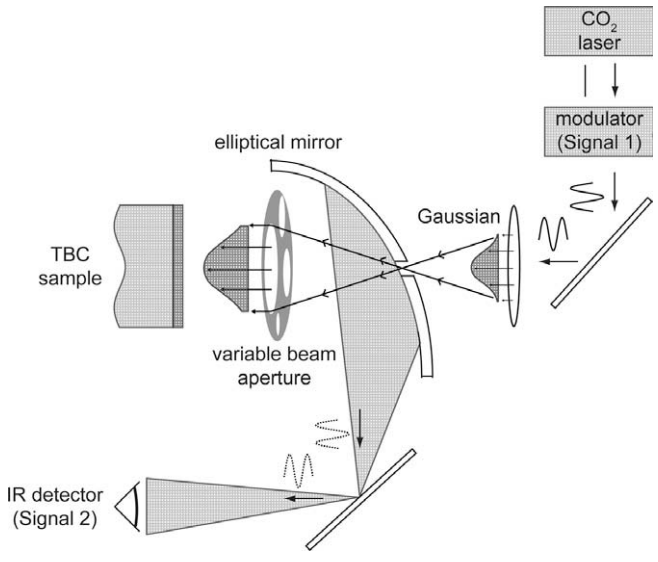

Fig. 1. Experimental arrangement for thermal properties measurement by the PopTea method (see text for details).

sion from the volume of the coating. Dimensionless thermal and radiative parameters are determined by nonlinear regression analysis of experimental data, yielding values for the thermal diffusivity, conductivity, density of the coating as well as the optical penetration depth [17]. Although the nominal measurement temperature was ambient, the actual coating temperature was higher (~65 °C) due to heating from the CO_2 laser.

2.3. Raman spectroscopy

Raman measurements were made at room temperature using a confocal Raman microprobe (LabRAM ARAMIS, HORIBA Jobin Yvon, NJ) with an excitation of 633 nm from a He–Ne laser. The spectral characteristics of the Raman spectra were evaluated by deconvolution of the Raman peaks using a commercial curve-fitting algorithm (LabSpec, HORIBA Jobin Yvon, NJ).

3. Results

Thermal property measurements, as well as Raman measurements, were first made on the thermal barrier coated superalloy coupons in their as-received condition and subsequently at periodic intervals during thermal cycling. This was continued until the coatings failed.

Fig. 2 shows the measurements of the phase of thermal emission with thermal cycling used in determining the thermal properties of the TBC presented in Fig. 3. While the thermal properties are obtained quantitatively as described in Ref. [16], the shape of the curves can be understood qualitatively as follows. As the thermal barrier coatings transmit into the near infrared, the thermal emission signal from the sample originates from both the thermal barrier coating and the underlying metal. The emission from the metal has a larger phase-lag because of the longer thermal diffusion path than from the coating itself. However, as the modulation frequency is increased, the thermal penetration depth for diffusion is reduced, until the emission from the

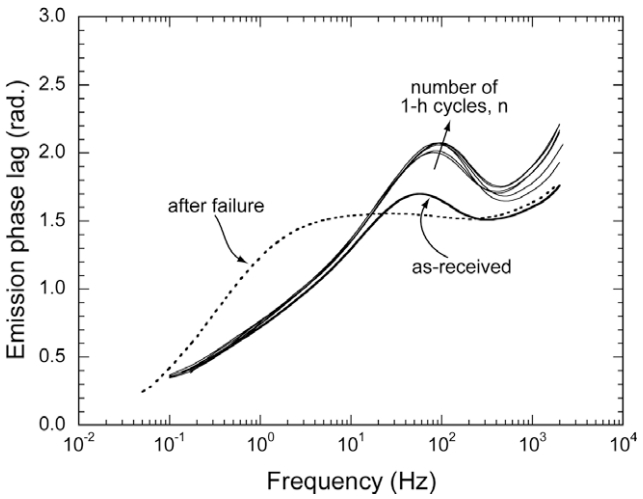

Fig. 2. Typical raw data obtained from the PopTea method.

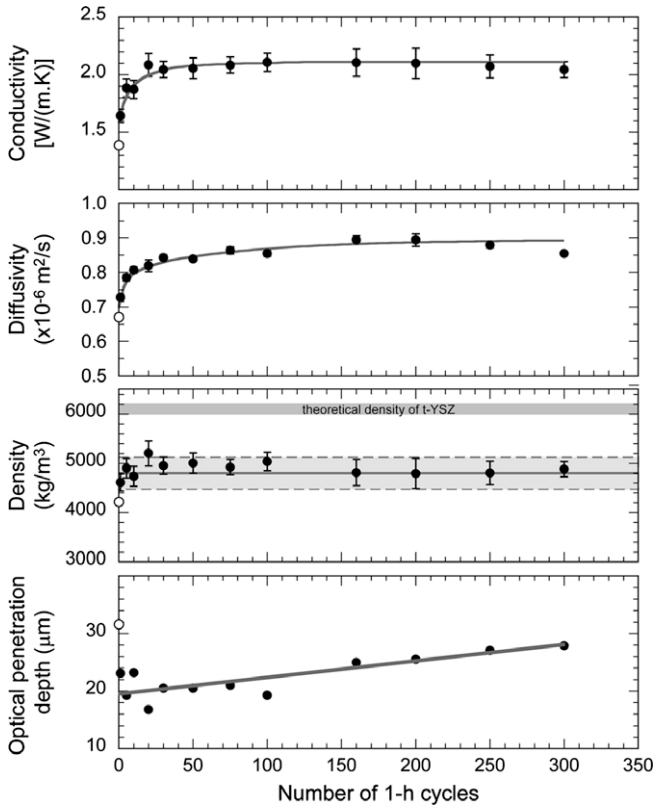

Fig. 3. Evolution of the thermal and physical properties of the coating with thermal cycling. The open circles represent the measurement of the as-deposited condition.

underlying metal is eventually cut-off at the highest frequencies. This competition results in the existence of the peak in the emission phase-lag curves shown in Fig. 2 since the large phase-lag emission contribution from the metal vanishes at the higher laser heating frequencies. The peak magnitude is proportional to the amplitude of the transient temperature field that penetrates to the metal. Therefore, the emission phase-lag curve and the peak grow with increasing thermal diffusivity of the coating material. This behavior is observed in Fig. 2 for the measurements made with increasing numbers of thermal cycles. Another feature of the emission phase curves, observed in Fig. 2, is the change that occurs when delamination occurs. The presence of a delamination disrupts the heat flow and cuts off emission from the underlying material and no distinct peak occurs. Wholesale delamination invalidates the heat transfer model used with the measurement, and hence no effort was made to extract the TBC properties after failure was noted. The other striking feature of the raw data in Fig. 2 is that the phase-lag curve for the as-received coating was significantly different to the curves after thermal cycling.

The evolution of thermal diffusivity, thermal conductivity and density of the TBC derived from analysis of the emission phase-lag curves are shown in Fig. 3, along with the laser optical penetration depth for the coating. The low thermal diffusivity of the as-deposited coating ($\alpha_{TBC} = 6.7 \times 10^{-7}$ m^2 s^{-1}) increased significantly during the first 20 cycles

at 1150 °C to 8.2×10^{-7} m^2 s^{-1}. This monotonic increase with number of cycles continued but at a much slower rate until 200 cycles, after which the diffusivity started to decrease. A similar trend was observed for the thermal conductivity with a significant increase observed during the first 20 h, increasing from 1.4 W m^{-1} K^{-1} in the as-deposited condition to 2.1 W m^{-1} K^{-1} after 20 cycles. Further exposure up to 300 cycles did not result in significant change in the thermal conductivity. Also, with the exception of the as-deposited condition, the density of the coating did not change with thermal cycling. The typical error in coating density determination was approximately 200 kg m^{-3}, i.e. 3.3% of the theoretical density, and so the difference in measured densities with cycling does not reveal a meaningful trend.

Raman spectroscopy indicated that there was no phase transformation to monoclinic in the coating even after 300 cycles (Fig. 4) since no Raman peaks characteristic of the monoclinic phase were detected. However, as noted previously, there is a progressive narrowing of the six distinct Raman bands, characteristic of tetragonal zirconia, and an increase in their peak symmetry, as was observed in an earlier study [13]. X-ray diffraction measurements of the coating after it had failed revealed that although there was no transformation to the monoclinic phase, there was some transformation from the original tetragonal-prime structure to the cubic phase (the Raman spectrum from the cubic phase is much weaker than from tetragonal). Together, these observations are consistent with the progressive thermal partitioning of the as-deposited tetragonal-prime phase into a mixture of cubic and tetragonal phases reported previously [13] and predicted in terms of the metastable phase diagram [18].

4. Discussion

Our results show that the thermal conductivity of EB-PVD 7YSZ-TBC coatings increase with thermal cycling between room temperature and 1150 °C, approaching an asymptotic value of ~2.1 W m^{-1} K^{-1}, significantly smaller than the conductivity of fully dense 7YSZ (~3 W m^{-1} K^{-1}). While the upper cycling temperature, 1150 °C, is considered rather low to observe a significant TBC densification, which would be an obvious reason for an increase in thermal conductivity with thermal cycling, our results show that the thermal diffusivity nevertheless increased significantly. A similar result has been found with EB-TBCs deposited on sapphire substrates [19]. In the following, possible explanations for the increase in thermal conductivity with thermal cycling are discussed. These include: (i) changes in shape of porosity, which can have the effect of altering the cross-section of material through which heat propagates and hence the heat flux density; (ii) changes in the intrinsic thermal conductivity as the metastable tetragonal-prime zirconia is annealed, (iii) changes due to phase partitioning, and (iv) changes in the TBC/thermally grown oxide (TGO) interface associated with TGO thickening and possible interface separations.

4.1. Microstructural changes

Two sets of data indicate that although there is no macroscopic densification, at least after the first cycle (Fig. 3), there are nevertheless microstructural changes in the coating even at 1150 °C. The first is the increase in optical penetration depth, measured at 10.6 micron, shown in Fig. 3. The second is the change in diffuse optical reflectance over the range 250–2500 nm (Fig. 5). Both sets of measurements are consistent with changes in the optical scattering from the coating, and hence microstructure, with thermal cycling. The former is at a wavelength longer than any characteristic microstructural length scale, and the latter spans the size of most of the pores. There are several characteristic features of the TBC microstructure that can cause optical scattering, including irregularly shaped pores within

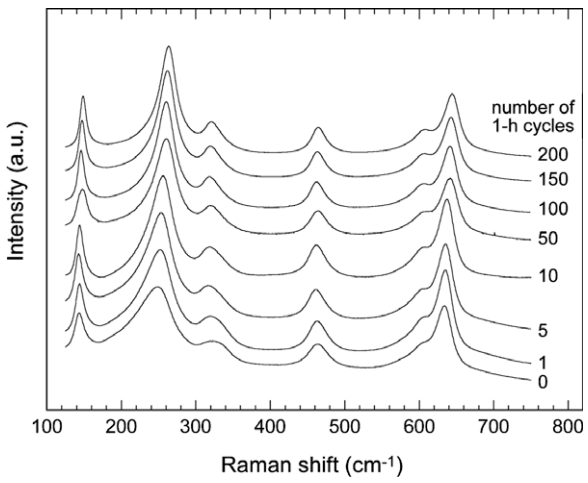

Fig. 4. Raman spectra taken after different numbers of thermal cycles showing tetragonal ZrO_2 phase.

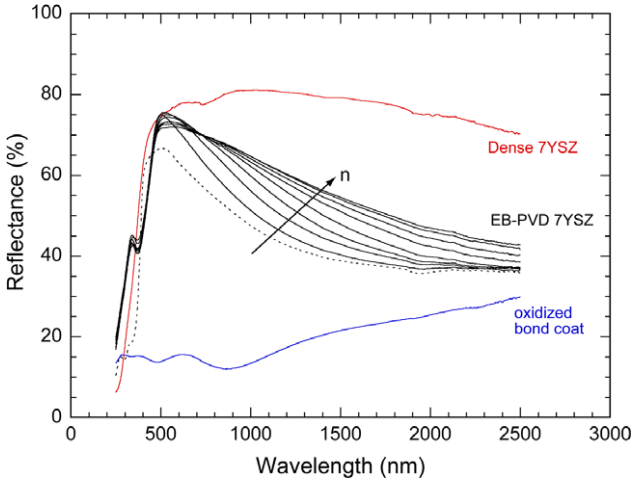

Fig. 5. Evolution of spectral diffuse reflectance of EB-PVD TBC with thermal cycling (n represents the number of 1 h cycles, from 0 to 200). The reflectance of the as-deposited coating is represented with a dashed line. The spectral reflectance of dense 7YSZ and oxidized bond coat are shown for comparison.

the individual columns, gaps between the columns, as well as the "feathery" surface of the columns themselves. These can all change at high temperatures via surface diffusion processes (Fig. 6) and hence are expected to be viable mechanisms at temperatures below which bulk diffusion occurs, namely at temperatures below which densification is significant. The decrease in diffuse scattering has been attributed to smoothening of the feathery structure in the TBC columns, the breaking up of crack-like gaps in the feathery structure of the columns and coalescence of nanoscale porosity inside the columns [20]. These are also consistent with several transmission electron microscopy observations of pore spherodization within the columns [21], as well as with our own work.

In considering the contribution of porosity, the thermal conductivity of a columnar TBC with heat flow parallel to the columns can be expressed as:

$$\kappa_{TBC} = f_{column}\kappa_{column} + (1 - f_{column})\kappa_{gap} \quad (1)$$

where f_{column} is the area fraction occupied by the TBC columns which have a thermal conductivity of κ_{column} and $(1 - f_{column})$ refers to the area fraction occupied by the intercolumnar gap. The thermal conductivity of the gap (κ_{gap}) filled with air is considered negligible, although this may in fact be significant under high-pressure conditions, such as in a high-pressure turbine. The thermal conductivity of the columns depends on both the volume fraction of internal porosity and the shape of the pores as well as their orientation with respect to the heat flow. Detailed calculations, such as those performed by Lu et al. [22], are necessary to determine the effect of all these geometric parameters on the conductivity. Nevertheless, the effect of pore spherodization is to increase the thermal conductivity by increasing the effective area though which heat can flow along the column. When the porosity is fully spherodized, the conductivity is given by the Rayleigh equation which for relatively small fractions, φ, of randomly distributed porosity is given by:

$$\kappa_{column} = \kappa_{dense}\left(1 - \frac{3\phi}{2}\right) \quad (2)$$

While there remains some uncertainty in the room temperature thermal conductivity of fully dense, tetragonal-prime zirconia, with values reported between 2.5 and 3.0 W m^{-1} K^{-1} [23–25], our work [4], as well as that of others, indicates that the correct value is the latter with the lower values most likely due to the presence of porosity. Using values for the area fraction of columns and internal porosity ($f_{column} = 0.9$ and $\varphi = 0.1$) used in Ref. [22], consistent with our own value for coating density shown in Fig. 3, the thermal conductivity of the coating and the columns are estimated to be ~2.3 and ~2.55 W m^{-1} K^{-1}, respectively. Lu et al. also calculated the thermal conductivity of an as-deposited EB-PVD coating taking into account the microstructural features, such as the rows of aligned ellipsoidal intracolumnar porosity inclined at an angle to the column axis as well as spherical pores, that they observed by electron microscopy. Using the same volume fractions for the porosities given above, they found that the conductivity was approximately 65–71% of that of dense zirconia, namely 1.95–2.13 W m^{-1} K^{-1}. Comparing this to the value for the completely spherodized coating (2.3 W m^{-1} K^{-1}), this calculation would indicate that pore spherodization accounts for approximately 0.17–0.35 W m^{-1} K^{-1}. Although it is recognized that this is a highly approximate estimate, it is significantly smaller than the increase we measure from ~1.4 W m^{-1} K^{-1} in the as-deposited condition to ~2.1 W m^{-1} K^{-1} after thermal cycling (Fig. 3). In turn, this difference suggests that while the thermal conductivity increase due to the change in pore morphology can be quite significant, it may not be sufficient to explain all the increase observed during thermal cycling. In the following section we discuss the possibility that the con-

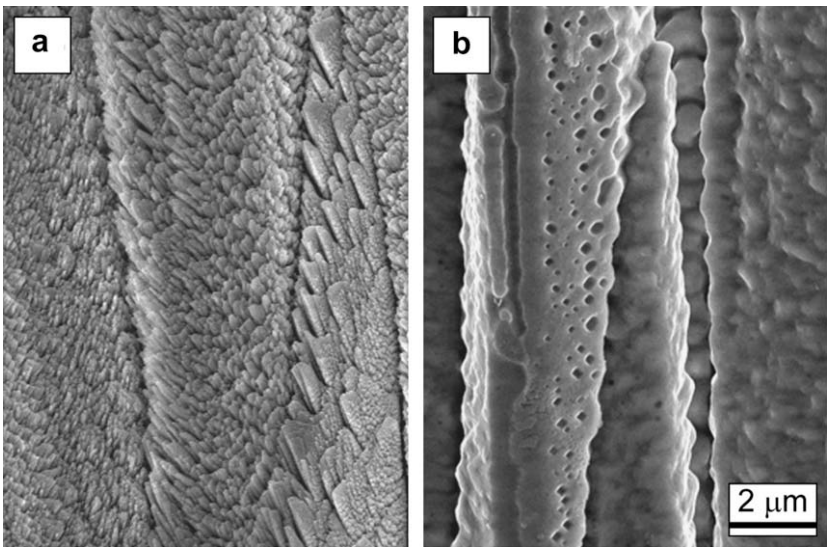

Fig. 6. Surface morphology of TBC columns in their as-deposited condition and after 350 1 h cycles at 1150 °C. The initial feathery structure evolves to a smoother surface and some large pores are observed in the TBC columns.

ductivity of the zirconia itself changes due to defect reduction upon annealing.

4.2. Changes in defect structure

The unusually low and temperature-independent thermal conductivity of yttria-stabilized zirconia above room temperature is due to defect phonon scattering, in particular scattering from the oxygen vacancies required to charge compensate for the Y^{3+} stabilizer. In EB-PVD coatings, deposited in their metastable tetragonal-prime phase, it is likely that other defects may also be present, such as clusters of point defects, cation defect dipoles, point defect ordering and planar defects [26]. As Raman spectroscopy is also sensitive to defects, the observed Raman peak narrowing suggests that thermal cycling not only alters the microstructure of the coatings but also lowers the concentration of point defects and hence increases the conductivity of the zirconia itself. To establish whether there was any correlation between them, the width of the Raman lines is plotted in Fig. 7 against the diffusivity and conductivity obtained from the PopTea measurements. As shown, a strong correlation is found. The three Raman bands of tetragonal ZrO_2, at 465 (E_g mode), 260 and 145 cm^{-1}, were selected because they are well separated in the spectra and also have large signal-to-noise ratios.

Although, as mentioned previously, the defects primarily responsible for the broadening of the Raman lines in zirconia have not been established, the narrowing of the bands suggests that the concentration of the defects decreases with thermal cycling. Furthermore, it is possible to make an argument for a correlation between the width of the Raman lines and the thermal conductivity as follows.

According to thermal conductivity models based on extension of the phonon analogy to the kinetic theory of gases, the lattice thermal conductivity is proportional to the mean phonon lifetime, τ, i.e. the time between phonon scattering events [27]. The Raman spectrum is related to the phonon spectrum of the lattice with energies of the different Raman bands corresponding to different phonon modes. The Raman (and infrared) spectra can, in turn, be interpreted in terms of damped harmonic oscillator models with the frequencies corresponding to the eigenmodes and the width of the lines, ΔE, proportional to the damping constants, γ. In general, the damping constants have units of the reciprocal of time, with $\gamma = \tau^{-1}$ [28]. Equivalently, from the energy–time uncertainty relation, the Raman line width is inversely proportional to the lifetime of the phonons and can be expressed as:

$$\Delta E = \frac{\hbar}{\tau} \tag{3}$$

where ΔE is the Raman line width in cm^{-1} and $\hbar$ is the Dirac constant. In a defective crystal, the phonon lifetime, τ, is related to the phonon lifetime in a perfect crystal, τ_A, associated with the intrinsic anharmonicity of the crystal, and the lifetime associated with defect scattering, τ_d, summed in parallel since they are parallel processes:

$$\frac{1}{\tau} = \frac{1}{\tau_A} + \frac{1}{\tau_d} \tag{4}$$

Consequently, defect scattering decreases the phonon lifetime, which, in turn, broadens the Raman line width. This suggests that the product of thermal conductivity and the width of the Raman lines is a constant, namely:

$$\kappa \Delta E = constant \tag{5}$$

This is consistent with the correlation observed in Fig. 7, with the strongest correlation between the two sets of measurements for the Raman modes at 260 and 465 cm^{-1}. The correlation is weaker for the mode at 145 cm^{-1} for reasons that are not yet clear but are probably related to the nature of these vibrational modes. Unfortunately, as there is still no consensus as to the nature of the Raman bands at 145 and 465 cm^{-1} [29–31], the energy dependence cannot be resolved at present.

There are two implications of the observed correlation. The first is the very good correlation between the width of the Raman bands with both thermal diffusivity and thermal conductivity. Also, the Raman scattering does not depend on porosity since it probes phonons in the crystal lattice, and the correlations suggest that the increase of thermal conductivity upon thermal cycling at 1150 °C is the result, at least in part, of changes in the "intrinsic" properties of the zirconia due to a decrease in the defect scattering with thermal cycling. It is emphasized, however, that the Raman signal does not provide any information about the changing contribution from changes in the shape and distribution of porosity. The second implication of this correlation is that it may provide an opportunity of monitor the evolution in thermal conductivity of zirconia-based TBCs using Raman spectroscopy, a non-destructive and non-contact method which does not require specimen prep-

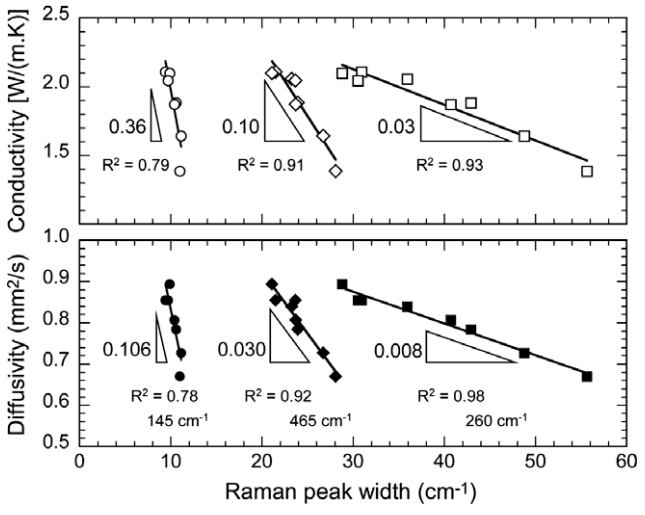

Fig. 7. Correlation between the evolution of width of the Raman bands indicated and the thermal diffusivity and conductivity of the coating.

aration and can be used to probe coatings on serviceable parts.

4.3. Effect of partial transformation

TBCs, whether deposited by EB-PVD or plasma-spraying, have the metastable tetragonal-prime structure, and over time at high temperatures partition slowly by diffusion of the Y^{3+} ion into a mixture of the equilibrium tetragonal phase, the equilibrium cubic phase and untransformed tetragonal-prime phase. At high temperatures, therefore, the microstructure evolves into a mixture of phases and the thermal conductivity is then a composite average of the individual phases and their spatial distribution. As far as we are aware this has not been considered previously. Our X-ray analysis indicates that after 350 cycles at 1150 °C, the coating contained a significant amount of cubic phase (Fig. 8), indicating that phase partitioning occurs even at this relatively low temperature. No monoclinic phase was detected, thereby indicating that the coating consists of three phases: tetragonal, cubic and tetragonal-prime. Taking $\kappa_{tetragonal} = 3.0\ W\ m^{-1}\ K^{-1}$ and $\kappa_{cubic} = 2.6\ W\ m^{-1}\ K^{-1}$ as the thermal conductivities of tetragonal and cubic zirconia, respectively [3], the bulk conductivity of this mixture (75% tetragonal + 25% cubic zirconia) is calculated to be 2.9 W $m^{-1}\ K^{-1}$. The difference between this value and the conductivity of tetragonal zirconia is rather small and is within the experimental uncertainty of our conductivity measurements. Thus, the effect of phase evolution on thermal conductivity evolution at 1150 °C is considered negligible compared to that of the changes in pore morphology and defect structure.

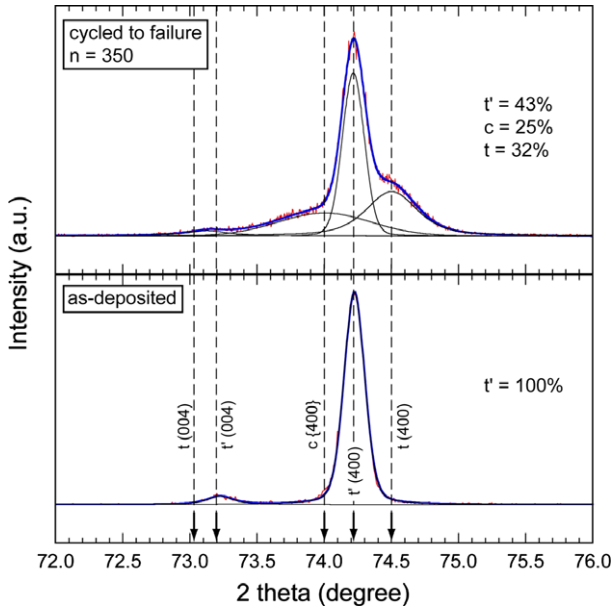

Fig. 8. Comparison of X-ray diffraction pattern of the coating in its as-deposited condition and after failure. By the time failure occurred, approximately 25% of the coating had transformed to the cubic phase.

4.4. Effect of interface separations

According to the data in Fig. 3, the thermal diffusivity of the coating decreased significantly after the longer exposures (250 and 300 cycles). A similar reduction in thermal conductivity has also been reported after annealing in air for 400 h at 1100 °C [9]. The authors of that work suggested that this might be due to changes in the substrate properties, including the growth of the TGO and the development of microcracks and local separation at the interface with the underlying alloy. Both would provide additional thermal resistance not included in thermal flash analysis models. Detailed microstructural analysis of cross-sections of the TBC/TGO interface of very similar coatings as in this work with cyclic

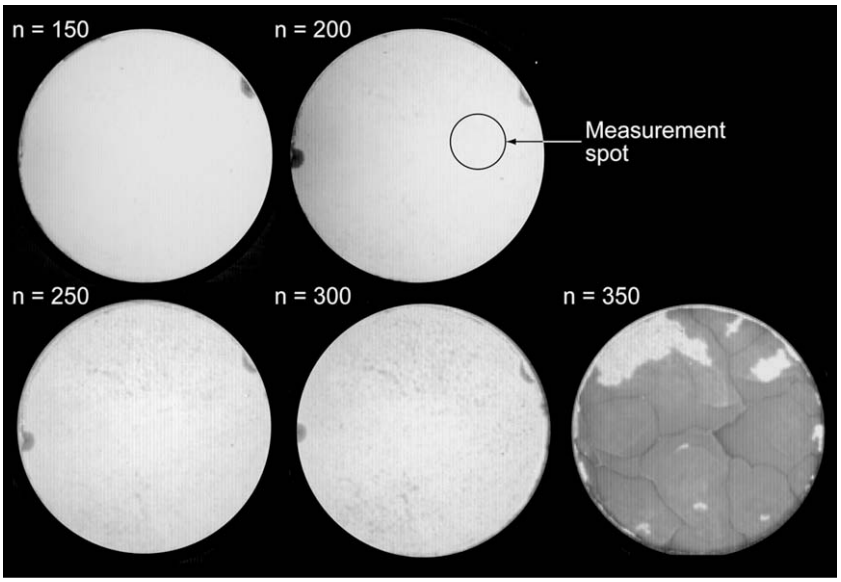

Fig. 9. Mid-infrared images of the TBC coupon showing local regions of coating delamination leading to complete spallation at failure. The local delaminations are seen as dark regions in the otherwise featureless bright image.

oxidation at 1150 °C indicates that local separations form, ranging in size from a few micrometers at the beginning of thermal cycling up to a few millimeters just before final TBC failure [32]. These were attributed to thermal cycling induced rumpling of the bond-coat.

To examine the possibility of local separation of the TBC/TGO interface affecting the derived values of the thermal conductivity, infrared images of the TBC were taken while the metal side was heated to 65 °C. In this imaging mode, separations at the TBC/TGO interface appear darker than those areas where the TBC was still intact. Due to the limited spatial resolution of our infrared camera, local separations (~1–2 mm in size) were not observed until after 250 cycles (Fig. 9). The number and size of these separations continued to increase until the TBC failed at 350 cycles, consistent with the findings of Tolpygo and Clarke [29]. However, despite the appearance of local separations, fitting to the raw data indicates that the added thermal resistance of these separations (prior to failure) is only a small fraction of the overall thermal resistance of the coating. This is consistent with the fact that while local separations may affect the thermal boundary conditions on which the PopTea analysis method is based, the separations only occur at times well after the thermal conductivity has apparently reached a limiting value.

5. Conclusions

It has been found that although EB-PVD ZrO_2-7 wt.% Y_2O_3 TBCs undergo negligible densification on cycling between room temperature and 1150 °C, their thermal diffusivity and thermal conductivity increased,rapidly at first, before slowly approaching a limiting value. The observed increase in thermal conductivity is attributed to two concurrent and parallel thermally activated processes. One involves microstructural changes, such as breaking up of irregularly shaped pores, smoothing of the feathery fine structure of the columns, and pore spherodization. The other is a decrease in the number of phonon scattering centers and possible defect ordering. A third possibility, that phase partitioning of the metastable tetragonal-prime structure into a mixture of phases can contribute to the changes in thermal conductivity, cannot be evaluated but is unlikely to be significant because of the similarity in thermal conductivities of the phases. A strong correlation is found between the narrowing of the Raman bands at 260 and 465 cm^{-1} and both the thermal diffusivity and thermal conductivity of the coatings. This suggests that Raman spectroscopy may be useful as a non-destructive, non-contact method for monitoring the changes in the thermal properties of TBCs.

Acknowledgments

This work was supported by the Office of Naval Research (for A.M.L. and D.R.C.) and by the University Turbine Systems Research Program (for T.R.K. and T.D.B.). The authors thank Dr. Ken Murphy (Howmet) for providing TBC coupons used in this study and Dr. Jesse Williams (UCSB) for advice on performing the X-ray diffraction measurements.

Appendix A. Uncertainties in the measurement of thermal properties by PopTea

When more than one coating property is determined, the uncertainty associated with fitting parameters is related to their uniqueness in describing the experimental data. When one coating property is intentionally changed from the "best-fit" value, the sum of the squared error will increase. Fig. A1a shows the increase in the sum of the squared error as the fitting parameter $a_{sub} = \sqrt{\alpha_{sub}}/\alpha_{coat}$ is forced from the best-fit value and the remaining parameters refitted to minimize the new sum of squared error. The extent to which the fit can be pushed away from the best-fit while remaining within the bounds of experimental error (5%) establishes uncertainty bounds on the fitted parameters. The

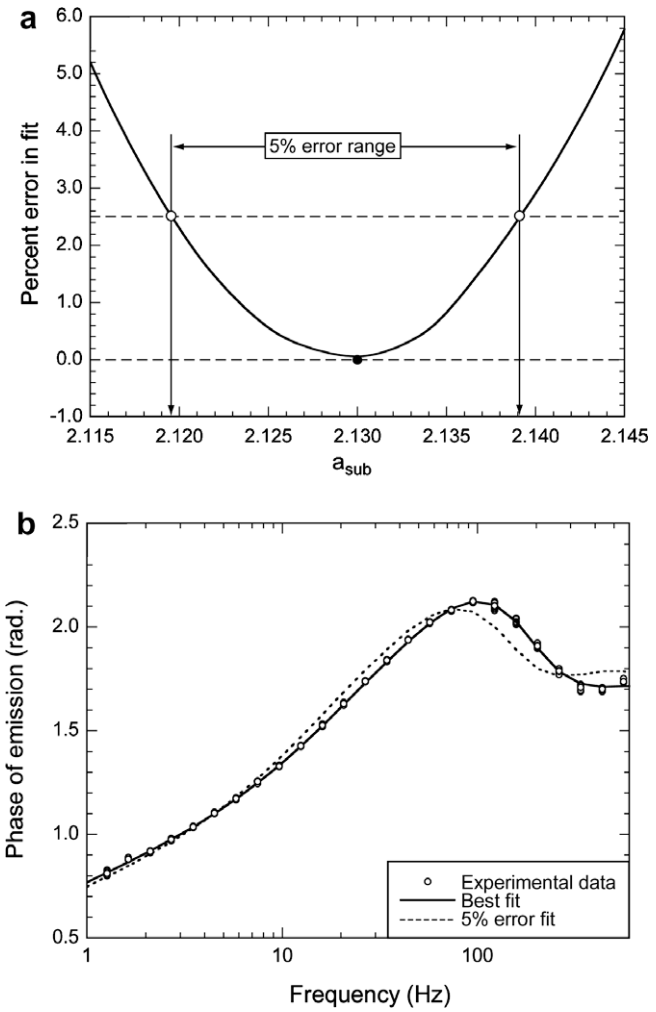

Fig. A1. Fitting uncertainty demonstrated for representative case of a coating after 50 cycles: (a) altering a_{sub} away from best-fit to demonstrate 5% error, and (b) an example of a 5% stray from best-fit produced with the model.

experimental error of 5% is appropriate if we see the effect this difference has on the fit (Fig. A1b). The dimensionless fitting parameters were treated in this way to determine their uncertainty. Dimensional thermal properties are directly dependent on two dimensionless parameters a_{sub} and γ as defined by the relations:

$$\alpha_{coat} = \frac{a_{sub}^2}{\alpha_{sub}} \tag{A.1a}$$

$$K_{coat} = \frac{k_{sub}}{a_{sub}\gamma} \tag{A.1b}$$

$$\rho_{coat} = \frac{[\rho C]_{sub}}{C_{coat}} \frac{a_{sub}}{\gamma} \tag{A.1c}$$

Uncertainty (u) in the dimensional parameters is then given by:

$$\frac{u_{\alpha_{coat}}}{\alpha_{coat}} = \sqrt{2\left(\frac{u_{a_{sub}}}{a_{sub}}\right)^2 + \left(\frac{u_{\alpha_{sub}}}{\alpha_{sub}}\right)^2} \tag{A.2a}$$

$$\frac{u_{k_{coat}}}{k_{coat}} = \sqrt{\left(\frac{u_{k_{sub}}}{k_{sub}}\right)^2 + \left(\frac{u_{a_{sub}}}{a_{sub}}\right)^2 + \left(\frac{u_\gamma{}^2}{\gamma}\right)} \tag{A.2b}$$

$$\frac{u_{\rho_{coat}}}{\rho_{coat}} = \sqrt{\left(\frac{u_{[\rho C]_{sub}}}{[\rho C_{sub}]}\right)^2 + \left(\frac{u_{C_{coat}}}{C_{coat}}\right)^2 + \left(\frac{u_{a_{sub}}}{a_{sub}}\right)^2 + \left(\frac{u_\gamma}{\gamma}\right)} \tag{A.2c}$$

Determination of errors in this work has assumed that the uncertainties in substrate properties are small compared to uncertainty in the fitted parameters. We have also assumed that the properties of the underlying superalloys do not change significantly with thermal cycling.

References

[1] National Research Council. Coatings for high-temperature structural materials: trends and opportunities. Washington, DC: National Academy of Sciences; 1996.
[2] Clarke DR, Levi CG. Ann Rev Mater Res 2003;33:383.
[3] Bisson JF, Fournier D, Poulain M, Lavigne O, Mevrel R. J Am Ceram Soc 2000;83:1993.
[4] Winter MR, Clarke DR. J Am Ceram Soc 2007;90:533.
[5] Zhu D, Miller RA, Nagaraj BA, Bruce RW. Surf Coat Technol 2001;138:1.
[6] Dutton R, Wheeler R, Ravichandran KS, An K. J Therm Spray Technol 2000;9:204.
[7] Wang H, Dinwiddie RB. Adv Eng Mater 2001;3:465.
[8] Azzopardi A, Mevrel R, Saint-Ramond B, Olson E, Stiller K. Surf Coat Technol 2004;177–178:131.
[9] Ratzer-Scheibe HJ, Schulz U. Surf Coat Technol 2007;201:7880.
[10] Lughi V, Tolpygo VK, Clarke DR. Mater Sci Eng A 2004;368:212.
[11] Zhu D, Miller RA. J Therm Spray Technol 2000;9:175.
[12] Bennett TD, Yu F. J Appl Phys 2005;97:013520.
[13] Lughi V, Clarke DR. J Am Ceram Soc 2005;88:2552.
[14] Tam AC. Rev Mod Phys 1986;58:381.
[15] Almond DP, Patel PM. Photothermal science and techniques. In: Dobbs ER, Palmer SB, editors. Physics and its applications. London: Chapman & Hall; 1996.
[16] Bennett TD, Kakuda T, Kulkarni A. J Appl Phys 2009;105:1.
[17] Bennett TD, Yu F. J Appl Phys 2005;98:093516.
[18] Fabrichnaya O, Wang Ch, Zinkevich M, Levi CG, Aldinger F. J Phase Equilib Diffus 2005;26:591.
[19] Limarga AM, Tolpygo VK, Clarke DR; in preparation.
[20] Limarga AM, Clarke DR. Inter J Appl Ceram Technol; in press, doi:10.1111/j.1744-7402.2008.02349.x.
[21] Renteria AF, Saruhan B. J Eur Ceram Soc 2006;26:2249.
[22] Lu TJ, Levi CG, Wadley HNG, Evans AG. J Am Ceram Soc 2001;84:2937.
[23] Nicholls JR, Lawson KJ, Johnstone A, Rickerby DS. Surf Coat Technol 2002;151–152:383.
[24] Raghavan S, Wang H, Dinwiddie RB, Porter WD, Mayo MJ. Scripta Mater 1998;39:1119.
[25] Schlichting KW, Padture NP, Klemens PG. J Mater Sci 2001;36:3003.
[26] Falkovsky LA. Phys Rev B 2001;64:024301.
[27] Klemens PG. In: Seitz F, Turnbull D, editors. Solid state physics. New York: Academic Press; 1958.
[28] Burns G. Solid state physics. New York: Academic Press; 1985.
[29] Feinberg A, Perry CH. J Phys Chem Solids 1981;42:513.
[30] Bouvier P, Gupta HC, Lucazeau G. J Phys Chem Solids 2001;62:873.
[31] Rignanese GM, Detraux F, Gonze X, Pasquarello A. Phys Rev B 2001;64:134301.
[32] Tolpygo VK, Clarke DR, Murphy KS. Surf Coat Technol 2004;188–189:62.